

See discussions, stats, and author profiles for this publication at: <https://www.researchgate.net/publication/230847603>

# Switching Off the Tackiness of a Nanocomposite Adhesive in 30 s via Infrared Sintering

ARTICLE in ACS APPLIED MATERIALS & INTERFACES · SEPTEMBER 2012

Impact Factor: 6.72 · DOI: 10.1021/am3013642 · Source: PubMed

CITATIONS

10

READS

21

8 AUTHORS, INCLUDING:



**Damien Dupin**

IK4-CIDETEC

37 PUBLICATIONS 815 CITATIONS

SEE PROFILE



**Juliana Nunes**

Universidade Federal do Rio Grande do Norte

8 PUBLICATIONS 78 CITATIONS

SEE PROFILE



**Steven P Armes**

The University of Sheffield

611 PUBLICATIONS 27,686 CITATIONS

SEE PROFILE

# Switching Off the Tackiness of a Nanocomposite Adhesive in 30 s via Infrared Sintering

Robert S. Gurney,<sup>†</sup> Damien Dupin,<sup>‡,§,#</sup> Juliana S. Nunes,<sup>‡</sup> Keltoum Ouzineb,<sup>§,||</sup> Elodie Siband,<sup>§</sup> José M. Asua,<sup>‡</sup> Steven P. Armes,<sup>‡</sup> and Joseph L. Keddie<sup>\*,†</sup>

<sup>†</sup>Department of Physics, University of Surrey, Guildford, Surrey, GU2 7XH, United Kingdom

<sup>§</sup>Cytec Surface Specialties, Anderlecht Strasse 33, B-1620 Drogenbos, Belgium

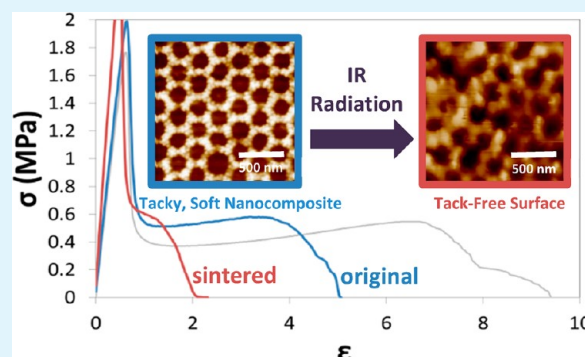
<sup>‡</sup>POLYMAT, and Grupo de Ingeniería Química, Departamento de Química Aplicada, Facultad de Ciencias Químicas, University of the Basque Country UPV/EHU, Joxe Mari Korta Zentroa, Tolosa Etorbidea 72, 20018 Donostia-San Sebastián, Spain

<sup>#</sup>Department of Chemistry, University of Sheffield, Dainton Building, Brook Hill, Sheffield, S3 7HF, United Kingdom

## S Supporting Information

**ABSTRACT:** Soft adhesives require an optimum balance of viscous and elastic properties. Adhesion is poor when the material is either too solidlike or too liquidlike. The ability to switch tack adhesion off at a desired time has many applications, such as in recycling, disassembly of electronics, and painless removal of wound dressings. Here, we describe a new strategy to switch off the tack adhesion in a model nanocomposite adhesive in which temperature is the trigger. The nanocomposite comprises hard methacrylic nanoparticles blended with a colloidal dispersion of soft copolymer particles. At relatively low volume fractions, the nanoparticles (50 nm diameter) accumulate near the film surface, where they pack around the larger soft particles (270 nm). The viscoelasticity of the nanocomposite is adjusted via the nanoparticle concentration. When the nanocomposite is heated above the glass transition temperature of the nanoparticles ( $T_g = 130\text{ }^\circ\text{C}$ ), they sinter together to create a rigid network that raises the elastic modulus at room temperature. The tackiness is switched off. Intense infrared radiation is used to heat the nanocomposites, leading to a fast temperature rise. Tack adhesion is switched off within 30 s in optimized compositions. These one-way switchable adhesives have the potential to be patterned through localized heating.

**KEYWORDS:** adhesion, self-assembly, sintering, nanoparticles, pressure-sensitive adhesive, latex



Pressure-sensitive adhesives (PSAs) adhere instantly and firmly to a substrate upon the application of light pressure. PSAs require an optimum balance of elastic and viscous properties in order to achieve strong adhesion.<sup>1</sup> A high tack adhesion energy arises not only from the thermodynamic work of adhesion at the interface with a substrate, but also from the bulk mechanical properties of the adhesive. The material must be liquidlike enough to flow at low strain rates to make conformal contact with a substrate and to achieve wetting. Additionally, the material must be solidlike enough to withstand shear stress, and viscoelastic so as to dissipate energy when being drawn at high strains during debonding. Strain hardening under large-strain deformation is desired for clean detachment from the substrate.<sup>2</sup> One of the few materials that meet these various conflicting requirements is a lightly cross-linked copolymer at a temperature well above its glass transition temperature,  $T_g$ . However, supramolecular networks have also recently been demonstrated to exhibit soft adhesion.<sup>3</sup>

For environmental and health reasons, there are increasing legislative demands for PSAs and polymer coatings to avoid the emission of organic solvents during processing.<sup>4,5</sup> Hence, there

has been greater reliance on PSAs prepared from aqueous colloidal dispersions of soft copolymer particles, *i.e.* latexes. Moreover, with increased emphasis on recycling and the reuse of materials, there is greater interest in adhesives that debond or “switch off” on demand, when triggered by an external stimulus. In “green” applications, switchable PSAs would allow the easy removal of adhesive labels and the clean recycling of packaging, and in principle enable the facile dis-assembly and reuse of electronic components.<sup>6</sup> In medical applications, the adhesion force during the removal of an adhesive from human skin correlates with the level of pain experienced by the patient.<sup>7</sup> Switchable adhesives ensure the painless removal of wound dressings from sensitive skin.<sup>8</sup>

The technical feasibility of switchable PSAs has been demonstrated using various external stimuli, including light, humidity and temperature. For example, the peel strength of methacrylate-functionalized adhesives containing a photo-

**Received:** July 18, 2012

**Accepted:** September 13, 2012

**Published:** September 13, 2012

initiator was reduced when they were irradiated under a halogen lamp, as a result of photoinitiated cross-linking that raised the elastic modulus.<sup>9</sup> When the light intensity was sufficiently high (>2000 lx) and the irradiation time exceeded five minutes, the polymer mobility was sharply reduced, resulting in almost complete loss of adhesion.<sup>10</sup> Two-way switching of adhesion has been obtained in coumarin-functionalized acrylate adhesives, whereby UVA radiation was used to switch off the adhesion, followed by UVC radiation to partially switch it back on.<sup>11</sup> For a light-switchable adhesive to be useful, it needs to be protected from light prior to switching, and the backing or the adherent must be transparent. In an alternative strategy, the ambient humidity has been used to adjust the surface composition of polymer blend films, which in turn modified the tack adhesion energy. However, in this case, the effect was relatively minor (less than a factor of 2).<sup>12</sup> There are numerous examples of the switchable wetting and adhesion of polymer brush surfaces using an external stimulus.<sup>13</sup> This strategy modifies the adherent surface but not the adhesive itself. For example, La Spina et al. used pH-responsive polymer brushes to create reversible adhesion in an aqueous solution.<sup>14</sup>

Switching adhesion off or on via a thermally induced surface phase transition is particularly attractive for medical adhesives.<sup>8</sup> Elsewhere, the shear strength of semicrystalline PSAs has been shown to drop sharply when they are heated above the crystal melting temperature.<sup>15</sup> In a liquid crystalline polymer, there is a transition between a nontacky and a tacky regime that occurs very abruptly at the smectic-to-isotropic phase transition temperature due to changes to the surface structure and wettability.<sup>16</sup> These examples of temperature-switchable adhesion are attractive, but they are not widely applicable, as they require specific chemical compositions and molecular architectures.

Ideally, a switchable adhesive should exhibit the following characteristics: (1) fast (preferably instantaneous) switching from tacky to nontacky states; (2) stability over time under standard temperature, illumination and humidity conditions; (3) reliance on standard adhesive materials without the need for the introduction of complicated and expensive chemical modifications; and (4) an ability to pattern surfaces to switch adhesion only within a desired region. In this work, nanocomposite adhesives were designed to offer these four desirable features. Additionally, the easy debonding of adhering surfaces is desirable, but this characteristic is not studied in the present work. The emphasis is on the switching off of the initial stickiness, referred to as tack.

It is well established that the bulk mechanical properties of colloidal nanocomposites can be conveniently tuned through the blending of glassy (i.e., hard) and rubbery (i.e., soft) particles.<sup>17</sup> This physical – rather than chemical – strategy does not require costly monomer synthesis or modifications of composition. In an important early work, Chevalier et al.<sup>18</sup> showed that hard polystyrene particles could be packed around soft particles as a means to control microstructure and the resulting mechanical properties. They found an increase in the elastic modulus above that predicted by mean-field theory when the nanocomposite was annealed above the  $T_g$  of the polystyrene particles. The sintering of the reinforcing hard particles created a stiff skeleton that raised the nanocomposite's elastic modulus. Their work nicely demonstrates a physical mechanism to “switch” a nanocomposite's mechanical properties.

In blends of colloidal particles of differing sizes, the continuous phase is determined by the relative size ratios and volume fractions of the constituents. As a general rule, smaller particles are able to pack around larger particles efficiently to create a continuous percolating phase at lower volume concentrations, compared to systems comprised of similar-size particles.<sup>19</sup> The effect of the volume fraction and particle size on the mechanical properties of high  $T_g$ /low  $T_g$  blends has been studied in depth<sup>20–22</sup> with application of the well-known Halpin–Tsai theory.<sup>23</sup>

Colloidal nanocomposites have been used in PSAs. Wang et al.<sup>24</sup> studied films made from blends of small, hard clay nanoparticles with large, soft polymer particles; they showed that the adhesive properties could be adjusted by varying the volume fraction of the hard phase. Bellamine and co-workers compared the effects of the addition of a hard nanoparticle phase or a cross-linking agent to a PSA, and found that both were able to increase shear resistance, while maintaining peel resistance.<sup>25</sup>

Elsewhere, it has been nicely demonstrated how the adhesion properties depend on the bulk properties of an adhesive polymer.<sup>2</sup> For example, the polymer typically should not have a storage shear modulus,  $G'$ , greater than 0.1 MPa at 1 Hz, or else it becomes too solid-like, according to the so-called Dahlquist criterion. Furthermore, the polymer must be sufficiently dissipative, as gauged by the ratio of the loss tangent over the shear modulus ( $\tan \delta/G'$ ). From this previous work, we expect that tack adhesion will be lost when the bulk properties of a nanocomposite are adjusted to lie outside of the acceptable range.

Here, we introduce a new strategy to achieve one-way switchable tack adhesion. By tuning the volume fraction of hard nanoparticles (NPs) in a colloidal nanocomposite, we optimize the adhesive properties of a PSA. Then, we sinter the percolating chains of hard NPs to transform them into a continuous percolating network (see Figure 1), which raises the elastic modulus above the Dahlquist criterion and thereby switches off the tack adhesion properties.

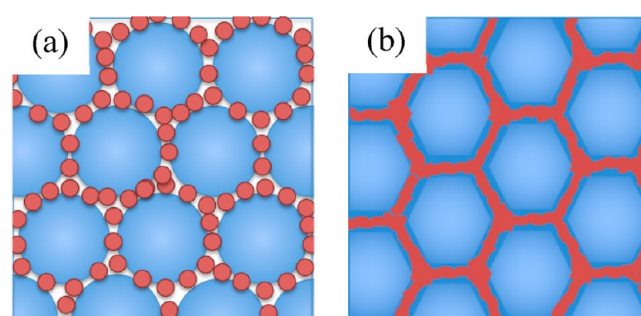


**Figure 1.** Two-dimensional graphical representation of a two-phase hard/soft particle blend. Hard nanoparticles (red) create a percolating network in the larger soft particles (blue). (a) Before sintering, the particles are separate but in physical contact. (b) After sintering, the particles are fused into a rigid network.

## RESULTS AND DISCUSSION

**Nanocomposite Structures.** Nanocomposite PSAs were created by blending hard nanoparticles with a colloidal dispersion of soft acrylate copolymer particles (called **P1** hereafter). For comparison, a more liquid-like copolymer (**P2**), which was synthesized with a chain transfer agent added to the

P1 composition, was also employed. One can consider P1 to be an optimized PSA, as its tensile storage modulus,  $E'$ , is precisely at the maximum limit where high tack adhesion is expected, according to the Dahlquist criterion,<sup>1</sup> and its value of  $\tan \delta/E'$  is relatively high (Table 1). (Note that for an incompressible

**Table 1. Physical Characteristic of Colloidal Particles**

latex description	P1, poly(butyl acrylate) copolymer	P2, poly(butyl acrylate) copolymer with CTA	NP, poly(methyl methacrylate-co-methacrylic acid) copolymer
CTA content (mol %)	0	0.05	0
DLS hydrodynamic diameter	270	225	52
DLS polydispersity	0.03	0.09	
solids content (wt %)	48 ± 1	52 ± 1	38 ± 1
gel fraction (%)	72 ± 6	67 ± 3	
$M_n$ (g/mol)	53 000	50 600	
$M_w$ (g/mol)	304 200	164 600	
$M_w/M_n$	5.7	3.2	
$T_g$ by DSC at 10 °C per min (°C)	−33.4	−34.2	130.0
$E'$ by DMA at 1 Hz, $T = 22$ °C (MPa)	0.33 ± 0.02	0.24 ± 0.02	2944 <sup>26</sup>
$E''$ by DMA at 1 Hz, $T = 22$ °C (MPa)	0.05 ± 0.02	0.11 ± 0.02	
$\tan \delta/E'$ at 1 Hz, $T = 22$ °C (MPa <sup>−1</sup> )	0.45	1.97	

substance,  $E'$  is related to  $G'$  by a factor of 3:  $E = 2G(1 + \nu)$ , where the Poisson ratio,  $\nu$ , is taken to be 0.5.) In comparison to P1, P2 has a lower storage modulus but a higher loss tangent. Thus, without the addition of hard nanoparticles, the properties of the P2 polymer are not in the right range to yield high adhesion energies.

We first consider the particle packing in dry films as the volume fraction of the hard nanoparticles is increased. Without the addition of NPs, an ordered hexagonal array of particles with residual particle/particle boundaries can be observed at the air/water interface (top) of dry films using AFM (Figure 2a). (For brevity, only phase images are presented in Figure 2 as they provide greater image contrast between the hard and soft particles compared to the height images. The corresponding height images are shown in Supporting Information, Figure S1). Hard NPs introduced at a small fraction (7.0 vol %) in the

adhesive pack in an ordered monolayer around the larger PSA particles at the film surface.

As the volume fraction of NPs increases, a “honeycomb” network of nanoparticles around the larger particles becomes more evident. NPs surround the PSA particles in a bilayer (11.6 vol %) and then multilayers at greater concentrations (16.4 vol %).

The area fraction of NPs at the air interface increases by a much greater extent than the overall volume fraction of NPs in the blend. This relationship is illustrated in Figure 3. If the

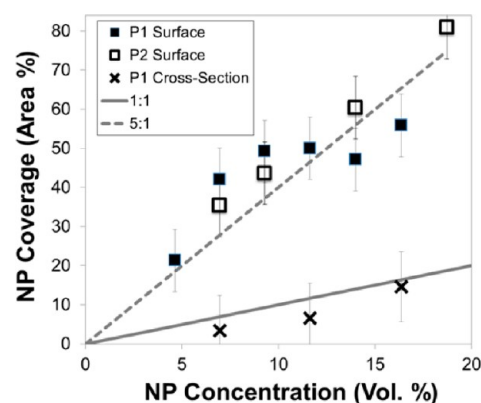


**Figure 3.** Relationship between the concentration of NPs in nanocomposite films and the area coverage at the top (air interface) and cross-section of the same films. For comparison, the solid line represents a 1:1 ratio, and the dashed line represents a 4:1 ratio.

surface structure is representative of the bulk composition, then a 1:1 ratio between the NP's area fraction at the air interface and the NP's volume fraction in the blend is expected. Instead, there is a ratio of approximately 4:1 between these two quantities, suggesting anisotropy within the film, with a greater accumulation of NPs at the air interface.

The NP arrangement at the air interface can be compared to what is found in the bulk of the film, as represented by the AFM images of the film cross sections, captured at the center of the film (Figure 2b). These images reveal a less regular arrangement of NPs. At low volume fractions, no honeycomb arrangement is observed. The number of NPs is depleted compared to what is expected for a 1:1 correlation between the

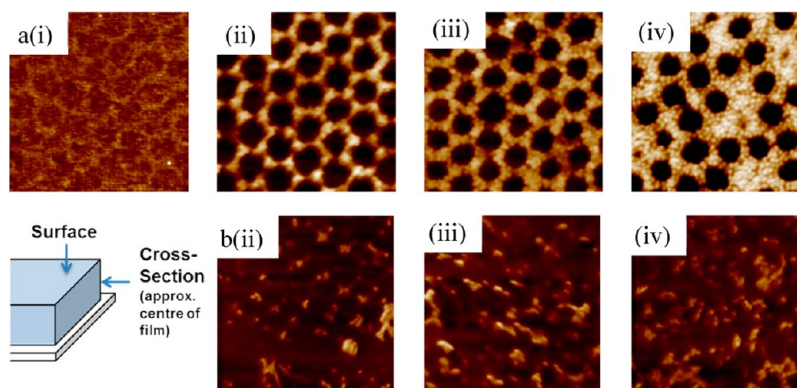


**Figure 2.** Evolution of the nanostructure of nanocomposite PSAs (using P1 polymer) as shown in AFM phase images of the (a, top row) air interface and (b, bottom row) cross-sections of films with varying NP concentration: (i) 0 vol % NPs; (ii) 7.0 vol % NPs; (iii) 11.6 vol % NPs; (iv) 16.4 vol % NPs. The larger PSA particles dissipate more energy during the intermittent contact of the AFM tip, and hence they appear darker in the images. The hard nanoparticles appear brighter. All images are 1.5  $\mu\text{m} \times 1.5 \mu\text{m}$ .



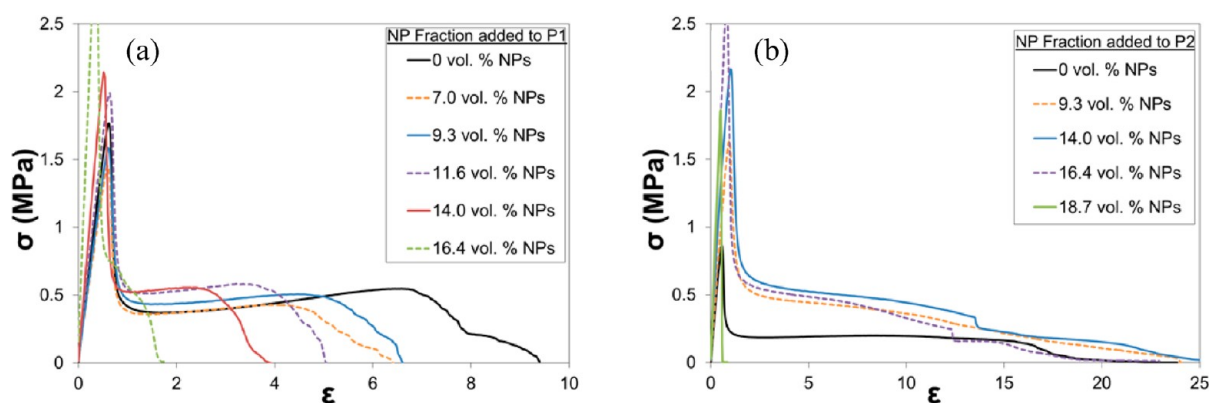


**Figure 4.** Representative probe tack curves show the effect of the addition of varying concentrations of hard nanoparticles to (a) P1 and (b) P2 PSAs.

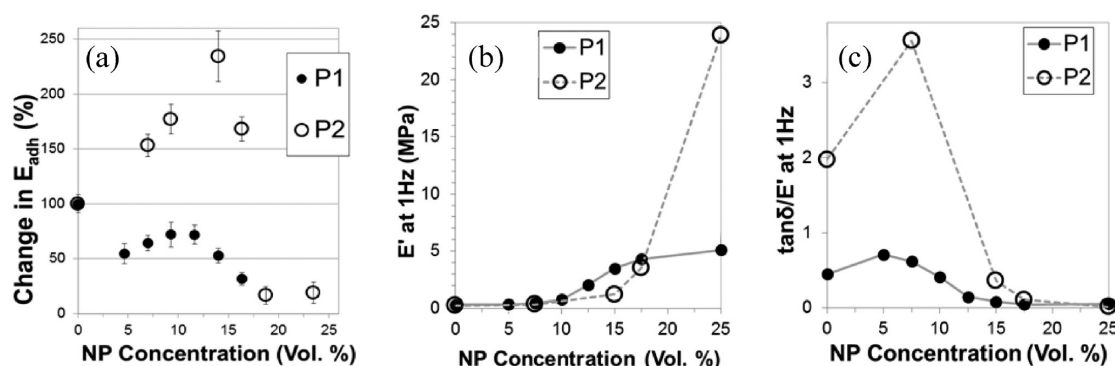


**Figure 5.** Effects of NP content on the bulk mechanical properties of soft nanocomposites made with the P1 and P2 soft polymers. Shown as a function of NP concentration for P1 and P2: (a) change in tack adhesion energy relative to the original PSA; (b) storage modulus,  $E'$  at a frequency of 1 Hz and at 22 °C, and (c)  $\tan\delta/E'$  at 1 Hz and 22 °C.

area fraction of particles in the cross-sectional image and the volume fraction in the blend (Figure 3). As the number of NPs in a blend must be conserved, a depletion in their composition in the bulk of the film is consistent with their accumulation near the original air interface. The nanostructure of softer P2 nanocomposites shows a similar trend with increasing NP concentration (see the Supporting Information, Figures S2 and S3).

When large and small colloidal particle blends are cast into films, stratification of the particles in the vertical direction can occur as a result of diffusional effects.<sup>27,28</sup> The diffusion coefficient determines the time it takes for particles to redistribute when they are accumulated at the top surface as a result of the evaporative loss of water. However, the slower-diffusing large particles are predicted in this model to accumulate at the top surface. The accumulation of NPs at the top surface of our colloidal blends is not expected from diffusional effects but is reminiscent of what was reported elsewhere by Luo et al.,<sup>29</sup> who described stratification of silica nanoparticles at the air interface, which they attributed to capillary-driven flow during film drying. In our experiments, the stratification could also be attributed to differences in the effective density of the two phases.<sup>30</sup> With an electric double layer, the effective density of the NPs will be lower than the density of the latex particles.

The idea of a stratified soft adhesive has been explored by Carelli et al.<sup>31</sup> who created adhesive bilayers by placing one adhesive film on top of another. They found that viscoelastic backing under an elastic surface layer was beneficial when

adhering to a high energy surface (i.e., steel), but detrimental for a low energy surface, i.e., polyethylene. As we will show later, the anisotropic structure of the nanocomposite PSAs is advantageous in achieving switching of the adhesion.

**Nanocomposite Adhesive Properties and Optimization.** The adhesive properties of the anisotropic films were determined through probe-tack analysis. The probe-tack method is a fundamental way to determine debonding mechanisms and adhesive properties,<sup>2</sup> and its results correlate well with the bulk factors that influence adhesion.<sup>32</sup> A probe is placed in contact with a PSA surface and removed at a constant velocity, so that the imposed stress ( $\sigma$ ) can be recorded as a function of the strain in the direction normal to the film ( $\epsilon$ ). In the case of a good PSA, cavities formed during debonding do not propagate as cracks but instead create thin walls that develop into extending fibrils. Ideally, upon maximum extension when strain hardening is observed, the fibrils will detach from the probe. If the material does not have sufficient strength and does not strain harden, cohesive failure is observed, whereby the fibrils thin and break to leave a residue on the probe. Fibrillation is the main contributing factor to the tack adhesion energy, and it is observed as a long stress plateau ( $\sigma_{plat}$ ) in the probe tack curve. The tack adhesion energy,  $E_{adh}$  (or work of adhesion) for a film of thickness  $l_0$  is calculated by

$$E_{adh} = l_0 \int_0^{\epsilon_{max}} \sigma(\epsilon) d\epsilon \quad (1)$$

Hence, it follows that a longer, higher plateau leads to a greater  $E_{adh}$ .

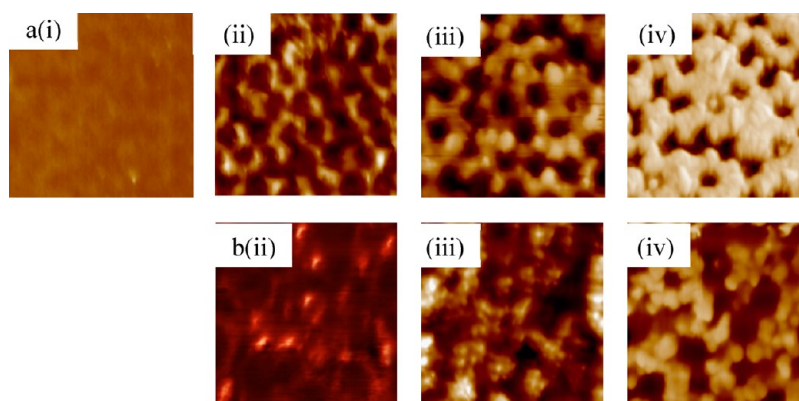


**Figure 6.** Evolution of the nanostructure of nanocomposite PSAs (using **P1** polymer) obtained after sintering, as shown in AFM phase images of the (a, top row) air interface and (b, bottom row) cross-sections of films with varying NP concentration: (i) 0 vol % NPs; (ii) 7.0 vol % NPs; (iii) 11.6 vol % NPs; (iv) 16.4 vol % NPs. The softer PSA phase appears darker, and the hard nanoparticles appear brighter in the images. All image areas are  $1.5 \mu\text{m} \times 1.5 \mu\text{m}$ . (Corresponding height images are shown in the Supporting Information, Figure S4.).

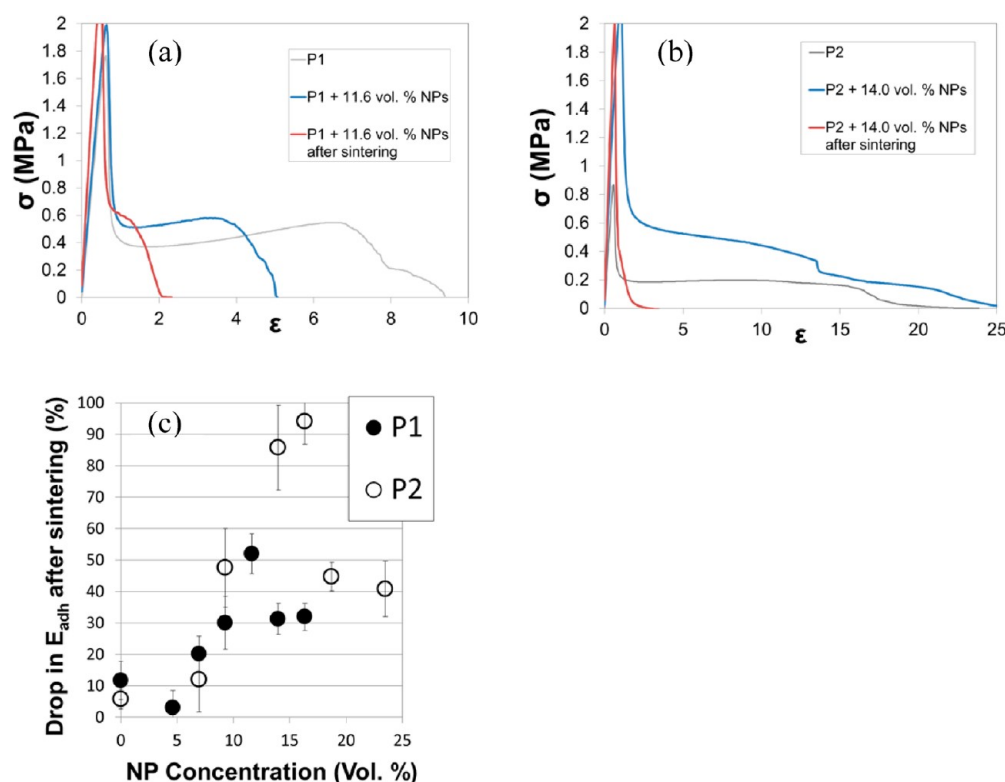


**Figure 7.** Representative probe tack curves illustrate the effect of the sintering optimal NP blends with (a) **P1** and (b) **P2** PSAs. (c) The percentage drop in tack adhesion energy after sintering as a function of nanoparticle content for **P1** (filled circle) and **P2** (unfilled circle).

Figure 4 compares the probe-tack curves obtained for the nanocomposites as the NP concentration is increased in each of the two PSA compositions. The softer **P2** material has a considerably lower fibrillation plateau compared to **P1**, which can be correlated with its lower elastic modulus.<sup>2</sup> We also note the clean detachment of **P1** (seen in the curve as a sharp end to the plateau), indicating adhesive debonding. By comparison, **P2** exhibits a gradual decay in the fibrillation plateau, indicating its cohesive failure. At lower concentrations, the NPs act as mobile fillers. For both types of nanocomposite PSA, there is a rise in  $\sigma_{\text{plat}}$  with increasing NP content, which indicates that the NP filler causes a hardening of the composite. This result is consistent with the findings reported elsewhere.<sup>24,25</sup>

The variation in the tack adhesion energy with increasing NP concentrations in each of the two PSAs is shown in Figure 5a. For **P1**, which is an already-optimized PSA, the tack adhesion energy is reduced to approximately 65% of its original value by the addition of NPs. Nevertheless, there is a local maximum in  $E_{\text{adh}}$  at around 10 vol % NPs. We observe that the addition of nanoparticles decreases the length of the plateau, which means that the fibrils are not being drawn as far, and hence  $E_{\text{adh}}$  decreases initially with nanoparticle addition. However, with the addition of nanoparticles, the composite hardens and the plateau stress increases, which results in a rise in  $E_{\text{adh}}$ .

For the nonoptimized **P2**, the addition of NPs raises  $E_{\text{adh}}$  to a maximum (which is 230% that of the original value) at an optimum concentration of around 14 vol % NPs. To interpret

further the effects of the added NPs on adhesion, the bulk mechanical properties of the nanocomposites are now considered.

There is a sharp rise in the storage modulus,  $E'$ , above NP concentrations of about 10 vol % in both the **P1** and **P2** nanocomposites (see Figure 5b). The Dahlquist criterion stipulates that  $E'$  must be below 0.3 MPa at 1 Hz for high tack adhesion. Hence the reduction in  $E_{\text{adh}}$  at higher NP concentrations can be explained.<sup>1,2</sup> The  $\tan \delta/E'$  ratio for the **P2** nanocomposite is consistently higher than for the **P1** nanocomposite (see Figure 5c). Hence, its greater viscoelasticity contributes to a longer fibrillation plateau at higher NP concentrations.

**Sintering to Achieve a Switch-off of Adhesion.** It is known that when colloidal polymer particles are heated above their  $T_g$ , they undergo coalescence via sintering.<sup>5</sup> The characteristic time required for sintering is proportional to the viscosity and hence inversely related to temperature. The extent of nanoparticle sintering was investigated with AFM analysis. After heating the nanocomposites to 140 °C for 30 min, the coalescence of the soft **P1** particles is observed (Figure 6a) and the boundaries between the particles disappear. At a NP concentration of 7.0 vol %, the NPs coalesce into “chainlike” structures across the film surface, but no longer appear to be in a continuous percolating “honeycomb.” At a concentration of 11.6 vol %, the sintered nanoparticles are arranged in a percolating honeycomb structure. At higher NP concentrations, as well as sintering and coalescence of the NPs, there is evidence for surface rearrangement, as the NPs cover the PSA particles almost completely. The bulk of the films, as represented in film cross-sectional images, provide similar results.

After the sintering process, the nanocomposites with a high NP concentration are no longer tacky. Small plastic pellets bounce off the sintered nanocomposite surface, whereas prior to sintering the same pellets adhere strongly (see video S1 in the Supporting Information). Probe-tack analysis confirms this qualitative observation that adhesion is switched off by sintering.

At NP concentrations below 10 vol %, probe-tack curves reveal that the NPs have not formed a sufficiently continuous chain to influence the tack properties. Instead, the NPs continue to act as a filler phase that has little effect on the adhesive properties after sintering (see the Supporting Information, Figure S5b). In intermediate ranges of NPs, where a continuous NP network is observed at the film surface, the fibrillation plateau length is reduced significantly after the NPs are sintered. At higher NP concentrations, there is no plateau whatsoever after sintering, thus reducing the tack adhesion energy to minimal values. The adhesion is switched off. The changes in the tack energy—attributed to the sintering process—are presented in Figure 7, where the percentage drops in adhesion after sintering are given. (The drop is defined relative to the initial value as  $E_{\text{adh}}(\text{initial}) - E_{\text{adh}}(\text{sintered})/E_{\text{adh}}(\text{initial})$ ). It is first important to note that both the plain **P1** and **P2** show a softening after heating (see the Supporting Information, Figures S5a and S6a). The loss in adhesion cannot be attributed to a hardening of the adhesive matrix. Furthermore, there is no evidence for a significant change in composition as a result of heating (see the Supporting Information, Figure S7).

There are notable differences between the switching of the softer **P2** nanocomposites and the **P1** nanocomposites. In **P2**, there is still a long fibrillation plateau and cohesive failure with

14.0 vol % NPs. After sintering this nanocomposite, the adhesion energy drops by 92%; adhesion is lost almost entirely. On the other hand, **P1** is closer to its optimum properties initially, such that the nanocomposite's adhesive performance is poorer with 11.6 vol % added NPs. Although the higher modulus raises  $\sigma_{\text{plat}}$ , the material is less viscoelastic and the plateau region is shortened. After sintering, there is evidence for only a limited extension of fibrils, and  $E_{\text{adh}}$  is significantly lower. These differences in the adhesion switch for **P1** and **P2** nanocomposites are apparent in Figure 7. The softer **P2** PSA can accommodate a greater amount of NPs without losing its adhesive properties and, in turn, the switch-off of adhesion is stronger upon sintering.

For practical applications, peel and loop tack tests are used to evaluate adhesives. Probe-tack energy usually correlates with the average peel force and the maximum loop tack force. In the peel test, an optimum peel force of 7.9 N/25 mm is found at 14.0 vol % for the **P1** nanocomposites, and it falls to around 0.8 N/25 mm after sintering. In the loop tack test, the optimum is 11.6 vol % NPs, but the loop tack force falls to about a sixth of its initial value after sintering. However, the loop tack force falls to zero after sintering with 14.0 vol % NPs (see the Supporting Information, Tables S1 and S2).

Figure 8 shows how the tensile storage modulus of the **P1** polymer differs after sintering as a function of increasing NP

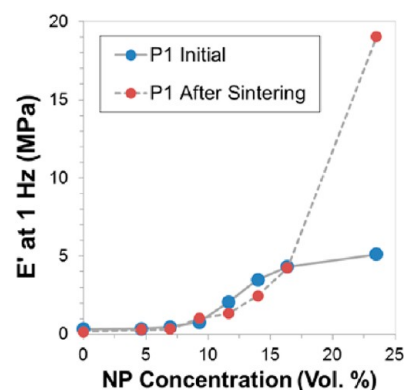


**Figure 8.** Storage modulus,  $E'$ , at 1 Hz for **P1** nanocomposites as a function of nanoparticle content, both before and after sintering.

concentration. Up to approximately 18 vol %, there is very little difference observed in the modulus before and after sintering. Our measurements of the bulk properties after sintering are not sensitive to the composition of surface layers, and hence there is very little difference in the moduli before and after sintering at low concentrations, when the NPs are below the percolation threshold at which they create a continuous chain. A continuous rigid skeleton in the nanocomposite cannot be made. Above 18 vol % NPs, there is a significant increase in the storage modulus after sintering. This is a strong indication that percolating NPs fused together to create a rigid skeleton. This observation prompted us to consider in greater detail how the nanoparticles are organized in the films and to construct the simple geometric models described in the next section.

#### Estimation of Particle Packing and Percolation Depth.

Given the high volume fraction of NPs near the film surface and the lack of NPs in the bulk material, we postulate that nanoparticles migrate to the surface under capillary flow during the drying stage, as has been proposed elsewhere.<sup>29</sup> The thickness of a surface layer containing nanoparticles depends on



how those nanoparticles are arranged around the larger soft particles. For example, the nanoparticles could form either a chain snaking around the soft particles, a monolayer, a bilayer or a multilayered structure, depending on the ratio of particle sizes and numbers.

Ottewill et al.<sup>33</sup> employed a simple method for calculating the volume of the encapsulating particular phase in the heterocoagulation of satellite particles around a single core particle. Here, using a similar approach, we estimate the number of satellite NPs able to surround a core particle by assuming the center of each NP lies upon an outer sphere of the combined radius of core and NP ( $r_c + r_{NP}$ , as shown in Figure 9). The number of NPs,  $n$ , able to fit on the surface area

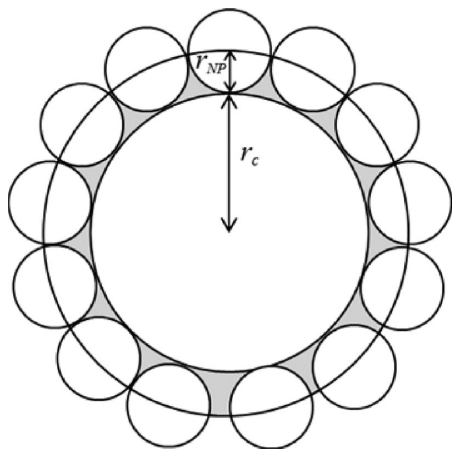


**Figure 9.** Diagram showing a cross-sectional view of satellite NPs (radius of  $r_{NP}$ ) surrounding a core particle ( $r_c$ ).

of this outer sphere is calculated by dividing its surface area by the cross-sectional area of the NP, giving

$$n = \frac{4f(r_c + r_{NP})^2}{r_{NP}} \quad ([2])$$

where  $f$  is the fraction of the area covered by the circular cross-section of spherical particles, which is  $(\pi)/(2\sqrt{3})$  for hexagonal close packing, assumed in this case.

For our P1 system ( $r_c = 135$  nm and  $r_{NP} = 26$  nm), we calculate that  $n = 139$  corresponds to a single NP layer. If each core particle had a layer surrounding it, then there would be a bilayer between the cores when they are close-packed in a film. To achieve a monolayer between the close-packed core particles, then only one-half as many NPs,  $n = 70$ , would be required. For a particular NP concentration, the total number of NPs in a unit volume of nanocomposite can be determined using this model.

When considering the fraction of NPs required to create a percolating network, it is possible to calculate, using various assumptions, a theoretical percolation threshold above which the small particles can be considered to be continuous. Kusy<sup>19</sup> derived an equation to calculate the volume fraction,  $V_c$ , of small dispersed particles required to form a continuous network around larger particles. To achieve continuity, the smaller dispersed particles only need to cover a fraction of the surface of the larger particles. The Kusy equation states that

$$V_c = 100[1 + (\phi/4X_c)(r_c/r_{NP})]^{-1} \quad ([3])$$

where  $\phi$  is a function of the packing arrangement of the smaller particles (taken to be 1.27 in our case, for a cubic lattice) and  $X_c$  is a function of the contact length occupied by the dispersed phase around the primary particle divided by the circumference of that particle, taken here to be 0.42 for a cubic lattice.<sup>19</sup>  $V_c$  for our system, with  $r_c/r_{NP} = 5.2$ , is estimated to be 19.7 vol %, which equates to  $n = 40$ .

The various values of  $n$ , corresponding to different packing configurations, can be used to estimate the number of “units” (composed of a core and NPs) that can be made in a film of arbitrary dimensions, given a particular NP volume fraction. Then, the volume of units can be found, and the thickness of the percolated layer (i.e., the film depth through which the nanoparticles completely surround the core particles for a given  $n$ ) follows. Figure 10 shows the estimated depth of a layer of

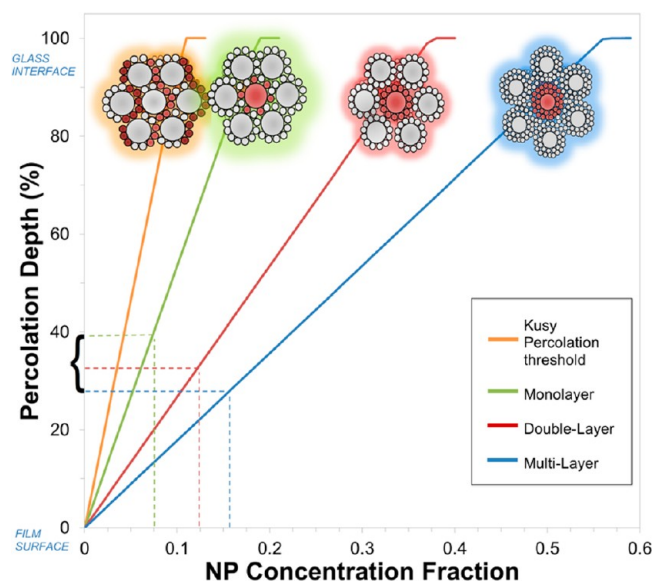


**Figure 10.** Estimate of the surface layer depth in which the nanoparticles are accumulated. Calculation of the percentage thickness of surface layer assumes different packing arrangements for the PSA-NP unit.

percolating or packed NPs for  $n = 40, 70, 139$ , and 209: the values of  $n$  required for the Kusy model, mono-, double-, and multilayers, respectively.

In AFM images in Figure 2, it is apparent that, more NPs pack around the larger soft particles as the NP concentration increases. At 7.0 vol % NPs, a monolayer of NPs is observed (corresponding to  $n = 70$ ). When the concentration increases to 11.6 vol % NPs, a particle bilayer is formed. Given this observation, we estimate in each case that the percolating layer is around 30–40% of the total thickness. This predicts that, beyond a depth of 40% of the film thickness, the film contains few nanoparticles. The model is thus supported by the cross-sectional AFM images in Figure 2. As their overall concentration in the dispersion is increased, the NPs accumulate in the top 30–40% of the film.

**Sintering Using IR Radiative Heating.** To be industrially relevant, the time to switch off the adhesion of a PSA should be as fast as possible. Thus we seek to extend the proof-of-concept data obtained through convection oven heating. In this section, we discuss the benefits of using radiative heating by an infrared source over conventional convective heating.



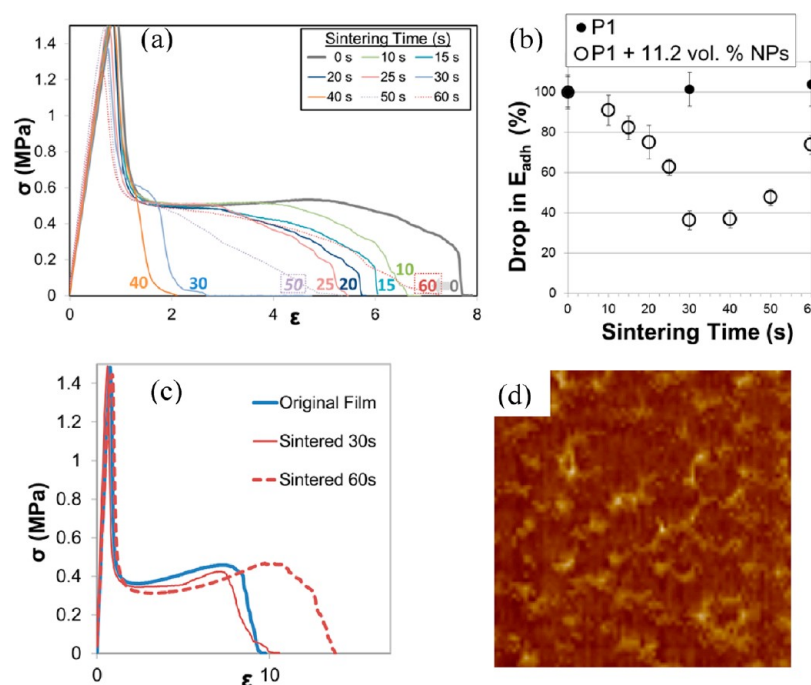


**Figure 11.** (a) Representative probe tack curves showing the effect of IR heating of **P1** nanocomposites (with 11.2 vol % NPs) for times ranging between 10 and 60 s. (b) Tack adhesion energy as a function of sintering time for **P1** (filled circles) and **P1** nanocomposite (open circles). (c) Representative probe tack curves showing the effect of IR heating for 30 and 60 s on pure **P1** PSA. (d) AFM phase image of the air interface of **P1** with 11.6 vol % NPs after 60 s of IR heating. Image area is  $1.5 \mu\text{m} \times 1.5 \mu\text{m}$ .

We postulated that the intense direct radiation from an IR emitter would heat up the nanocomposite PSA films more efficiently and to a higher temperature, thus achieving the same sintering effect in a much shorter time. In research reported elsewhere,<sup>34</sup> IR radiative heating was demonstrated to induce the sintering of hard latex particles. An IR emitter at full power was placed at a distance of 3 cm from the **P1** nanocomposite surface. The adhesives were radiated for various lengths of time.

Figure 11a shows the effect of increasing the time under the IR lamp from 10 s to one minute on the tack curves of the radiated nanocomposites. With increasing radiation times, the length of the plateau decreases, indicating a reduction in fibril extension, as is seen in Figure 7. An optimal switch-off of adhesion, comparable to that achieved in the convection oven (over 90% reduction in adhesion), is achieved after just 40 s of radiation. For this radiation time, there is no fibrillation plateau and there is no deformation of the nanocomposite when the probe is debonded. In Figure 11b, we note that there is a linear reduction in adhesion energy for IR sintering times between 10 and 25 s, whereas a low  $E_{adh}$  (with no fibrillation, and thus considered a switch-off) is achieved for sintering times of 30 s or longer.

Monitoring the nanocomposite temperature during IR radiation reveals that  $140^\circ\text{C}$  is reached in approximately six seconds. The nanocomposite thus requires only a few seconds above the  $T_g$  of the hard nanoparticles before coalescence occurs. About 30 s is required for this coalescence to become sufficient to switch off adhesion. The fact that the NP layer is situated at the top of the film may aid this process, since only the top part of the film needs to be sufficiently irradiated to coalesce, thereby facilitating the switch-off.

As a control experiment, a film of plain **P1** was exposed to IR radiation under the same conditions. IR radiative heating has a negligible effect on the **P1** tack energy (see Figure 11b) but

does influence the tack debonding curve, with the adhesive showing signs of softening, as opposed to the hardening seen in the nanocomposites (see Figure 11c). When the nanocomposite is heated for longer than 40 s, there is an increase in the tack adhesion energy, with the tack curves showing a more liquidlike response (with a gently downward sloping plateau and cohesive failure). This result indicates softening of the polymer occurs under prolonged radiation and shows that extended heating should be avoided. A likely explanation is that under IR irradiation, the very high temperatures (greater than  $250^\circ\text{C}$  according to in situ measurements) significantly reduce the viscosity of the soft polymer phase. The NP particles are then able to be submerged under the film surface, so as to reduce the surface energy. Without the hard particles at the surface, the adhesive displays a more liquidlike response. The surface restructuring takes time, and its effects are not seen when the IR heating is for only 30 s.

AFM analysis supports this explanation. Figure 11d shows that the number of NPs of a **P1** nanocomposite after IR heating for 60s is significantly lower than what was seen after heating in an oven at  $140^\circ\text{C}$  (cf. Figure 6a, iii). Image analysis reveals that the NP surface coverage drops from over 40 area % initially to  $13 \pm 2$  area % after IR heating.

## CONCLUSIONS

We have demonstrated how hard polymer nanoparticles can be used to adjust the adhesion characteristics of a PSA composed of a soft copolymer latex. When the nanoparticles are added to a liquidlike polymer, the viscoelastic balance can be optimized, such that the tack adhesion energy increases to more than 200% of its initial value. When the optimized nanocomposites are heated, the nanoparticles sinter together to create a reinforcing structure, which switches off adhesion and reduces the tack energy by 90%. The hard nanoparticles are

concentrated in the near-surface region, possibly because of capillary-driven flow. Consequently, an NP fraction below the theoretical percolation threshold of the bulk material can be used. The anisotropy in properties (normal to the adhesive surface) is ideal for an adhesive that needs to remain adhered to one substrate while debonding from the other.

The loss of the tack adhesion energy after sintering is explained by an increase in the elastic modulus at the film surface. Compared to adhesive systems that rely on melting transitions or cross-linking reactions, the switchable nanocomposite described herein simply uses conventional colloidal particles, which is likely to be much more cost-effective.

In initial experiments, the nanocomposite adhesives were heated for 30 min in a convection oven at a temperature that is approximately 10 °C above the  $T_g$  of the nanoparticles. In subsequent experiments, the films were sintered using IR radiation. The tack adhesion energy was significantly reduced after heating for times as short as 30 s, which is faster than previous reports for photoinitiated cross-linking switches. Our switching mechanism does not require special polymer chain architecture or composition; it is applicable to any glassy polymers.

We propose that it should be possible to heat a pressure-sensitive adhesive in specified regions, perhaps through the use of an infrared laser or a shadow mask,<sup>35</sup> such that the adhesion is switched off locally. Thus, lateral modulation of the IR radiation across a homogeneous nanocomposite adhesive could be used to produce tacky and nontacky patterned regions on mm length scales. Furthermore, IR absorbers could be added to raise the temperatures and the rate of heating,<sup>36,37</sup> to achieve a faster switch. This study also provides a note of caution when exposing such adhesive polymer nanocomposites to elevated temperatures, since adhesive switch-off could well occur unintentionally. Nevertheless, the adhesion of the nanocomposite PSAs will not be lost at temperatures below the NP  $T_g$  where sintering will not occur. In summary, the nanocomposite adhesives offer advantages of being (1) relatively fast in switching to nontack, (2) stable at room temperature and under standard lighting, (3) using standard thermoplastic polymers in a simple process, and (4) potentially able to be patterned.

## METHODS

**Synthesis of Standard PSA Latexes.** P1 latex was synthesized using a semi continuous emulsion polymerization. Deionized water and 40 nm seed particles were added to a reactor equipped with a double-jacket heated at 83 °C. Separately, a pre-emulsion of monomer was prepared by adding deionized water, surfactants, a buffer and a monomer mixture. The monomer mixture is based on n-butyl acrylate, acrylic acid, methyl methacrylate, and ethyl acrylate. When the reactor temperature reached 83 °C, an aqueous solution of sodium persulfate and the pre-emulsion were added simultaneously over 4 h. After complete addition of the pre-emulsion and the initiator solution, the reactor was cooled down and the latex dispersion was filtered to estimate the coagulum and placed in jars. The recipe for the P2 latex was as for P1 apart from the inclusion of dodecyl mercaptan to the monomer composition to act as a transfer agent to reduce the molecular weight.

**Synthesis of the P(MMA-co-MAA) nanoparticles (NP).** P(MMA-co-MAA) nanoparticles were prepared using semicontinuous emulsion polymerization. In this method, 2.40 g of sodium dodecyl sulfate (SDS, 98.5%, Sigma-Aldrich) and 470 g of water were added to a glass reactor equipped with a stainless steel stirrer, a reflux condenser, a sampling device, a nitrogen gas inlet tube and a temperature probe. When the reaction temperature reached 80 °C, a

shot of initiator solution (0.32 g of ammonium persulfate (APS, ≥ 98%, Aldrich) and 10 g of water) was added. Then, 305 g of the monomer mixture (15.25 g of methacrylic acid (MAA, 98.0%, Sigma-Aldrich) and 289.75 g of methyl methacrylate, MMA, Quimidroga) was fed very slowly over 8 h. At a polymerization time of 3 h (≈ 18% solids content), a surfactant solution feed (comprising 11.27 g Dowfax 2A-1 (alkyldiphenyloxide disulfonate, 45 wt % solution, Dow) in 35 g water) was started. At the end of the monomer feed, the reaction was maintained at 80 °C for more than 60 min in order to obtain a high final monomer conversion. Deionized water was used.

During the reaction, samples were withdrawn at regular interval times, and the reaction was stopped by the addition of a drop of a 1 wt % aqueous hydroquinone (Merck) solution. Samples were characterized regarding solids content and particle size. Solids content was determined by gravimetry. The average particle size (Z-average) of the polymeric nanoparticles was measured by dynamic light scattering (DLS) with a Zetasizer Nano ZS apparatus (Malvern Instruments). Before the analysis, the samples were diluted with deionized water in order to avoid multiple scattering. The value was obtained from the average of two repeated measurements. According to the manufacturer, for a well-dispersed and stable sample, the accuracy and precision of the measurements should be within 2%.

**Polymer Blend Preparation.** The nanoparticles were blended dropwise with the P1 and P2 latexes at various concentrations. Blends were mixed using a magnetic stir bar for 30 min, agitated for a further 2 h, and allowed to settle for 30 min before use.

**Probe-Tack Adhesion Analysis.** For probe-tack measurements, the dispersions were cast on glass substrates using a cube applicator and dried at room temperature for 8 h. To sinter the nanoparticles, the films were heated for 30 min at 140 °C in a convection oven with air flow. Films were then removed to fresh air and allowed to cool to room temperature (over a two hour period) before use. Thermogravimetric analysis (see the Supporting Information, Figure S7) indicates that there is a mass loss of less than 0.5 wt % in both the pure P1 and nanocomposite samples when heating to 140 °C in air. This mass is attributed to residual water from the film formation process. All of the dried films had thicknesses ranging from 80 to 100 μm, according to measurements with digital calipers, averaged over approximately ten measurements. In later experiments, films were heated using a 4 kW carbon IR emitter (Heraeus Noblelight). This IR source has a maximum power of 150 kW/m<sup>2</sup>. At its maximum power, the emitter has a temperature of 1200 °C, corresponding to peak emission wavelength of 2 μm. It has a very fast response time such that it reaches its maximum temperature within 1–2 s.

Probe-tack adhesive analysis of the nanocomposite films on glass plates followed the Avery method (MicroSystems Texture Analyzer, Godalming, UK) using a spherical (2.54 cm diameter) steel probe. The probe was lowered onto the film with a load of 4.9 N and allowed 1 s of contact before being withdrawn from the film surface at a constant velocity of 0.1 mm s<sup>-1</sup> which corresponds to an initial strain rate of 1 s<sup>-1</sup>. For each sample, four or five replicate measurements were made.

**Glass Transition Temperature.** Small pellet-like samples were prepared for thermal analysis by drop-casting 1 mL droplets on silicone-coated paper and drying in air for 8 h. The droplets were further dried in an oven at 105 °C with airflow for 3 min, after which they were removed to fresh air, and allowed to cool for 2 h before analysis. The glass transition temperature of each latex was found by differential scanning calorimetry (Q1000 TA Instruments, New Castle, DE, USA) at a heating rate of 10 °C/min in nitrogen.  $T_g$  was calculated using TA Instruments Universal Analyzer software, using the midpoint of the step in heat flow.

**Dynamic Mechanical Analysis.** Nanocomposite specimens for dynamic mechanical analysis (DMA) were obtained by casting the wet latex in poly(tetra fluoroethylene) PTFE molds and drying for seven days, after which they followed the same drying process as for films cast on glass substrates. Strips (15 mm × 3 mm × 1.5 mm) were cut from the films for DMA. When the ends of the strips were clamped in a tensile geometry, the central portion under strain was 10 mm long.

DMA of these strip samples was performed using a commercial instrument (Q800, TA Instruments, New Castle, DE, USA) in

isothermal tensile mode at 22 °C with a strain of 0.1% at a frequency of 1 Hz, which is comparable to the strain rate used in the probe-tack measurements.

**AFM Imaging.** For topographic imaging, dispersions were cast on 50  $\mu\text{m}$  polypropylene sheets using a spiral bar coater, and followed the same drying process as for films cast on glass substrates. For cross-section AFM imaging, a sheet of PET (50  $\mu\text{m}$  thick) was laminated onto the sample, with pressure applied from a 2 kg roller. Samples were cut to 10 mm  $\times$  10 mm and attached to a silicon substrate, which was in turn attached to a metallic base plate.

Cross-sections of films were cut using a Diatome Cryo-Immuno 3 mm diamond knife with a cryogenically cooled microtome (Nova Ultratome microtome) under liquid nitrogen, and attached to a glass plate perpendicular to the silicon substrate, bonded with silver paint. The AFM measurements were conducted in tapping mode on an NT-MDT Ntegra Prima atomic force microscope, using a Nanosensors PPP-NCH-W silicon cantilever with a resonance frequency of  $\sim$ 300 Hz, force constant of between 10 and 130 N/m and set point ratio (ratio of free oscillation magnitude to landed magnitude) of 0.75.

Height and phase images of 3  $\mu\text{m}$   $\times$  3  $\mu\text{m}$  were recorded, and are displayed after third order 2-D flattening correction using Nova NT-MDT scanning probe microscopy software. Images of the film cross sections were captured toward the center of the film.

To calculate the surface coverage of nanoparticles, images were converted to binary masks using ImageJ (version 1.42) image editing software from the United States National Institutes of Health (<http://rsb.info.nih.gov/ij/>). The binary mask was created using a Renyi entropy thresholding method to identify the phase image color threshold between hard and soft particles. Errors on these area measurements are taken from the mean difference between the upper and lower threshold limits. For analysis of the top surfaces, three different areas on each sample were selected, and the overall error was calculated.

## ■ ASSOCIATED CONTENT

### ■ Supporting Information

AFM height images of surfaces and cross sections of nanocomposite films, before and after sintering. Probe-tack data for P1 and P2 nanocomposites, before and after sintering. Peel and loop-tack data for nanocomposites before and after sintering. A video demonstrating adhesion of nanocomposites, before and after sintering. Thermogravimetric data for P1 and a P1 nanocomposite heated to 150 °C. This material is available free of charge via the Internet at <http://pubs.acs.org>.

## ■ AUTHOR INFORMATION

### Corresponding Author

\*E-mail: j.keddie@surrey.ac.uk.

### Present Addresses

<sup>#</sup>Dpto. Nuevos Materiales IK4-CIDETEC, Parque Tecnológico de San Sebastián, Paseo Miramón, 196, 20009 Donostia - San Sebastián, Spain

<sup>||</sup>Toray Films Europe, St. Maurice de Beynost, 01708 Miribel Cedex, France

### Notes

The authors declare no competing financial interest.

## ■ ACKNOWLEDGMENTS

The manuscript was written through contributions of all authors. All authors have given approval to the final version of the manuscript. We gratefully acknowledge funding from Cytec Surface Specialties, Engineering and Physics Sciences Research Council (EPSRC) and METRC for the PhD studentship of RG. We also acknowledge the EPSRC Knowledge Transfer Account (KTA) at the University of Sheffield for partial

funding of DD's industrial secondment. We thank V. Doukova, C.-H. Lei, and A. Georgiadis (University of Surrey) for experimental assistance.

## ■ REFERENCES

- (1) Dahlquist, C. A. *Treatise on Adhesion and Adhesives: Vol. 2: Materials*; Patrick, R. L., Ed.; Marcel Dekker: New York, 1969; pp 219–260.
- (2) Deplace, F.; Carelli, C.; Mariot, S.; Retsos, H.; Chateauminois, A.; Ouzineb, K.; Creton, C. *J. Adhes.* **2009**, *85*, 18–54.
- (3) Courtois, J.; Baroudi, I.; Nouvel, N.; Degrandi, E.; Pensec, S.; Ducouret, G.; Chanéac, C.; Bouteiller, L.; Creton, C. *Adv. Funct. Mater.* **2010**, *20*, 1803–1811.
- (4) Jotischky, H. *Surf. Coat. Int., Part B: Coat. Trans.* **2001**, *84*, 11–20.
- (5) Keddie, J. L.; Routh, A. F. *Fundamentals of Latex Film Formation: Processes and Properties*; Springer: New York, 2010.
- (6) Murray, C. T.; Rudman, R. L.; Sabade, M. B.; V., P. A. *MRS Bull.* **2003**, *28*, 449–454.
- (7) Klode, J.; Schöttler, L.; Stoffels, I.; Körber, A.; Schadendorf, D.; Dissemond, J. *J. Eur. Acad. Dermatol. Venereol.* **2011**, *25*, 933–939.
- (8) Chivers, R. A. *Int. J. Adhes. Adhes.* **2001**, *21*, 381–388.
- (9) Webster, I. *Int. J. Adhes. Adhes.* **1999**, *19*, 29–34.
- (10) Boyne, J. M.; Millan, E. J.; Webster, I. *Int. J. Adhes. Adhes.* **2001**, *21*, 49–53.
- (11) Trenor, S. R.; Long, T. E.; Love, B. J. *J. Adhes.* **2005**, *81*, 213–229.
- (12) Diethert, A.; Ecker, K.; Peykova, Y.; Willenbacher, N.; Müller-Buschbaum, P. *Appl. Mater. Interfaces* **2011**, *3*, 2012–21.
- (13) Stuart, M. A. C.; Huck, W. T. S.; Genzer, J.; Müller, M.; Ober, C.; Stamm, M.; Sukhorukov, G. B.; Szleifer, I.; Tsukruk, V. V.; Urban, M. W.; Winnik, F.; Zauscher, S.; Luzinov, I.; Minko, S. *Nat. Mater.* **2010**, *9*, 101–13.
- (14) La Spina, R.; Tomlinson, M. R.; Ruiz-Pérez, L.; Chiche, A.; Langridge, S.; Geoghegan, M. *Angew. Chem., Int. Ed.* **2007**, *46*, 6460–3.
- (15) Agirre, A.; de las Heras-Alarcón, C.; Wang, T.; Keddie, J. L.; Asua, J. M. *ACS Appl. Mater. Interfaces* **2010**, *2*, 443–51.
- (16) de Crevoisier, G.; Fabre, P.; Corpart, J. *Science* **1999**, *285*, 1246–1249.
- (17) Wang, T.; Lei, C.-H.; Dalton, A. B.; Creton, C.; Lin, Y.; Fernando, K. A. S.; Sun, Y.; Manea, M.; Asua, J. M.; Keddie, J. L. *Adv. Mater.* **2006**, *18*, 2730–2734.
- (18) Chevalier, Y.; Hidalgo, M.; Cavaillé, J. Y.; Cabane, B. *Macromolecules* **1999**, *32*, 7887–7896.
- (19) Kusy, R. P. *J. Appl. Phys.* **1977**, *48*, 5301–5305.
- (20) Pukanszky, B.; Tudos, F. *Makromol. Chem.* **1990**, *191*, 221–231.
- (21) Vidovska, D.; Maurer, F. H. J. *Compos. Interfaces* **2006**, *13*, 819–830.
- (22) Colombini, D.; Hassander, H.; Karlsson, O. *Macromolecules* **2004**, *37*, 6865–6873.
- (23) Halpin, J. C.; Kardos, J. L. *Polym. Eng. Sci.* **1976**, *16*, 344–352.
- (24) Wang, T.; Colver, P. J.; Bon, S. A. F.; Keddie, J. L. *Soft Matter* **2009**, *5*, 3842–3849.
- (25) Bellamine, A.; Degrandi, E.; Gerst, M.; Stark, R.; Beyers, C.; Creton, C. *Macromol. Mater. Eng.* **2011**, *296*, 31–41.
- (26) *Polymer Data Handbook*; Mark, J. E., Ed.; 2nd Editio.; Oxford University Press: New York, NY, 1999.
- (27) Nikiforow, I.; Alexander, M. K.; Langhoff, A.; Pohl, K.; Turshatov, A.; Johannsmann, D. *Langmuir* **2010**, *26*, 13162–13167.
- (28) Trueman, R. E.; Lago Domingues, E.; Emmett, S. N.; Murray, M. W.; Keddie, J. L.; Routh, A. F. *Langmuir* **2012**, *28*, 3420–8.
- (29) Luo, H.; Cardinal, C. M.; Scriven, L. E.; Francis, L. F. *Langmuir* **2008**, *24*, 5552–61.
- (30) González Serrano, C.; McDermott, J. J.; Velegol, D. *Nat. Mater.* **2011**, *10*, 716–21.
- (31) Carelli, C.; Déplace, F.; Boissonnet, L.; Creton, C. *J. Adhes.* **2007**, *83*, 491–505.

- (32) Shull, K. R.; Creton, C. *J. Polym. Sci., Part B: Polym. Phys.* **2004**, *42*, 4023–4043.
- (33) Ottewill, R. H.; Schofield, A. B.; Waters, J. A.; Williams, N. S. J. *Colloid Polym. Sci.* **1997**, *275*, 274–283.
- (34) Georgiadis, A.; Bryant, P.; Murray, M.; Beharrell, P.; Keddie, J. L. *Langmuir* **2011**, 2176–2180.
- (35) Georgiadis, A.; Routh, A. F.; Murray, M. W.; Keddie, J. L. *Soft Matter* **2011**, *7*, 11098–11102.
- (36) Li, F.; Winnik, M. A.; Matvienko, A.; Mandelis, A. J. *Mater. Chem.* **2007**, *17*, 4309.
- (37) Cingil, H. E.; Balmer, J. A.; Armes, S. P.; Bain, P. S. *Polym. Chem.* **2010**, *1*, 1323.